The impact of a hot sodium ion population on the growth of the Kelvin-Helmholtz instability in Mercury's magnetotail

P. W. Gingell,[1] T. Sundberg,[1] D. Burgess,[1]

Corresponding author: P. W. Gingell, School of Physics and Astronomy, Queen Mary University of London, Mile End Road, London, E1 4NS, UK. (p.w.gingell@qmul.ac.uk)

[1]School of Physics and Astronomy, Queen Mary University of London, Mile End Road, London, E1 4NS, UK.

Abstract.

Observations of Mercury's local plasma environment by MESSENGER have revealed that the planet hosts a strongly asymmetric magnetosphere as a result of an off-axis dipolar or quadrupolar internal field and significant finite Larmor radius effects at the boundary layer between magnetospheric and solar wind plasma environments. One important asymmetry appears in the growth and evolution of Kelvin-Helmholtz (K-H) waves at the dawn and dusk flanks of the magnetopause. Linear analysis and global hybrid simulations support a dusk-dawn asymmetry in the growth rate caused by finite Larmor radius effects, and indeed K-H waves have been almost exclusively observed at the dusk magnetopause during northward IMF. Observations of these K-H waves at sodium gyro-scales invites investigation into the impact of the hot planetary sodium ion population, itself distributed preferentially on the dusk flank, on the growth of the K-H instability and associated plasma transport. We present local two-dimensional hybrid simulations of the dusk and dawn boundary layer, with varying magnetospheric sodium ion number density, and examine the associated changes in the growth rates of the K-H instability, K-H wave spectra, and cross-boundary particle transport. We show that gyroresonance between growing K-H vortices and sodium ion gyration introduces a strong spectral peak at sodium gyro-scales at the dusk magnetopause, that an increase in sodium ion number density increases dawn-dusk asymmetry of K-H growth rates, and that cross-boundary particle transport decreases with sodium number density at the dawn flank.

1. Introduction

Fly-bys and the orbital campaign of the MErcury Surface, Space ENvironment, GEochemistry, and Ranging (MESSENGER) spacecraft have revealed that Mercury hosts a magnetosphere that is in many respects an analogue of the terrestrial system [Zurbuchen et al., 2008; Slavin et al., 2008]. However, a combination of small system size, low intrinsic magnetic field strength and high solar wind density makes the Hermean local plasma environment an extreme and highly dynamic system [Slavin et al., 2009]. Major asymmetries in the system are introduced by effects relating to an off-axis dipolar or quadrupolar intrinsic field [Anderson et al., 2008], and ion gyro-scales on the order of the system size. Hence, Mercury's plasma environment presents a useful laboratory for the study of kinetic and time-dependent plasma processes.

The study presented in this paper focuses on the growth and evolution of the Kelvin-Helmholtz (K-H) instability driven by shear flows at the flanks of Mercury's magnetopause. K-H waves have also been observed in several other systems, including Venus [Pope et al., 2009], Saturn [Masters et al., 2009, 2010; Delamere et al., 2011] and Earth [Chen & Kivelson, 1993; Chen et al., 1993; Kokubun et al., 1994; Fairfield et al., 2000, 2003, 2007; Otto & Fairfield, 2000; Farrugia et al., 2000; Hasegawa et al., 2004]. Given the local plasma parameters, the instability is expected to have a much more significant effect on the Hermean system than the terrestrial magnetosphere [Sundberg et al., 2010]. The instability is also expected to play an important role in cross-boundary transport of solar wind and magnetospheric ions, and structure formation in the magnetotail [Huba, 1996; Hasegawa et al., 2004; Gingell et al., 2014]. Observations by the MESSENGER spacecraft have revealed that Kelvin-Helmholtz waves are found almost exclusively in the dusk flank of the magnetosphere during northward interplanetary magnetic field (IMF) [Sundberg et al., 2012; Liljeblad et al., 2014], and are characterised by sawtooth oscillations in the equatorial components of the magnetic field [Boardsen et al., 2010], which can be reconstructed to demonstrate the emergence of shear vortices [Sundberg et al., 2011]. The growth of the Kelvin-Helmholtz instability is favoured for conditions which minimise the field line tension in the streaming direction [Chandrasekhar, 1961], i.e. for northward IMF (parallel to the planetary field) and southward IMF (antiparallel). However, weak or no signatures of the instability are present at both flanks during southward IMF. This can be attributed to disruption of the boundary layer by reconnection at the dayside [Hwang et al., 2011]. Given the small system size and Mercury's weak dipole, the dawn-dusk symmetry breaking can be attributed to gyration of protons and heavier ions of exospheric origin.

It is well established that ion gyration has an important effect on the growth rate of the Kelvin-Helmholtz instability at ion-scale shear boundaries[Nagano, 1979; Thomas & Winske, 1991, 1993; Thomas, 1995; Huba, 1996]. However, the nature of the effect is strongly dependent on the initial conditions and plasma beta [Huba, 1996]. Early analytic results suggested that the co-rotating boundary, at which the background magnetic field and vorticity at the shear layer are parallel, would have a faster growth rate for Kelvin-Helmholtz waves than the counter-rotating boundary, at which the background magnetic field and vorticity are antiparallel [Nagano, 1979]. However, more recent numerical results suggest that widening of the co-rotating boundary (required by the kinetic equilibrium) leads to a faster growth rate at the counter-rotating boundary than the co-rotating boundary [Nakamura et al., 2010]. Global hybrid simulations of Mercury's magnetosphere [Trávníček et al., 2009; Paral & Rankin, 2013] and observations by MESSENGER [Sundberg et al., 2012] appear to support the latter result: the growth of Kelvin-Helmholtz instability is faster on the counter-rotating, dusk flank during northward IMF.

A spectral analysis of Kelvin-Helmholtz waves at the dusk flank of the magnetopause has revealed an apparent bias towards the growth of K-H vortices at scales associated with the gyration of a hot sodium ion population [Gershman et al., 2015], created by ionisation of exospheric neutrals at the dayside, sub-solar region [Zurbuchen et al., 2008, 2011; Raines et al., 2011; Gershman et al., 2014]. This suggests that the gyration of sodium ions plays an important role in the evolution of the K-H instability, despite its relatively low number density.

For the first time, we investigate the effect of the hot sodium ion population on the growth of the K-H instability at the flanks of Mercury's magnetotail by means of local, two-dimensional hybrid simulations. We find that gyro-resonance between sodium ions and growing Kelvin-Helmholtz vortices produces strong peaks in K-H wave spectra at sodium gyro-scales at the dusk, counter-rotating shear boundary, and suppresses growth of the instability at the dawn, co-rotating shear boundary. We use test particle simulations to investigate the gyro-resonance mechanism, which we suggest is due to the combined current of petal-like orbits of trapped counter-rotating sodium ions. We also present measurements of cross-boundary transport and mixing coefficients for the sodium ion and proton populations, which are relevant to investigations of magnetospheric ion distributions and exospheric loss.

2. Simulations

We investigate the evolution of ion scale shear boundaries by means of simulations utilizing a hybrid model, which combines a kinetic, particle-in-cell treatment of ion species with a charge-neutralising, massless and adiabatic electron fluid [Matthews, 1994]. Maxwell's equations are solved under the low-frequency Darwin limit, neglecting collisions and with zero resistivity. The simulations presented in this paper are two-dimensional in configuration space, with 3 vector components for fields and velocities (e.g. $B_{x,y,z}(x,y,t)$), and periodic boundary conditions in both x- and y-dimensions.

Simulations are initialised with two parallel velocity shear boundaries separating a high density solar wind proton population and a lower density magnetospheric proton and sodium ion populations. The number densities $n_s(x)$ for each species are initialised as follows:

$$T(x) = \frac{1}{2}\left[\tanh\left(\frac{x-x_0}{L}\right) - \tanh\left(\frac{x-x_1}{L}\right)\right] \quad (1)$$

$$n_{\mathrm{msp}}(x) = n_0^{\mathrm{msp}} T(x) \quad (2)$$

$$n_{\mathrm{Na}}(x) = n_0^{\mathrm{Na}} T(x) \quad (3)$$

$$n_{\mathrm{swp}}(x) = n_0^{\mathrm{swp}}\left(1 - T(x)\right), \quad (4)$$

for boundary layers of width L at $x = x_0$ and $x = x_1$, with the magnetospheric populations dominating for $x_0 < x < x_1$, and the solar wind population dominating for $x < x_0$ and $x > x_1$. Each population s is initialised with shear velocity $\mathbf{U}_s = (0, u_s, 0)$ relative to the simulation frame, and thermal velocity $v_{\mathrm{th}}^{\mathrm{s}}$. The parameters n_0^s determine the relative densities of each species. The magnetic field is initialised as uniform and perpendicular to the grid, $\mathbf{B} = (0, 0, B_0)$, such that we can neglect the effects of changing magnetic topology via reconnection. Using futher simulations including a small, uniform in-plane field component $B_y = 0.05B_0$, we have verified that the main results concerning K-H growth and spectral properties are unchanged from the perpendicular field cases. The conclusions drawn from this study relating to the search for a mechanism for sodium gyro-resonance are therefore unaffected by the additional physical processes introduced by this geometry. The parameters B_0, n_0^{s} and $v_{\mathrm{th}}^{\mathrm{s}}$ are chosen such that the boundary layer is initialised in MHD pressure balance. We note that low amplitude magnetoacoustic waves propagate from the boundary at $t = 0$ as a result of the deviation from full kinetic equilibrium [Henri et al., 2013; Cerri et al., 2013]. Simulations are normalised such that the reference background number density $n_0 = 1$, $B_0 = 1$, and spatial scales are given in units of the proton inertial length $d_p = v_A/\Omega$, for $v_A = B_0/\sqrt{\mu_0 m_p n_0}$, and time scales are given in units of the inverse proton gyrofrequency $t_\Omega = \Omega^{-1} = (eB_0/m_p)^{-1}$ respectively. Ion thermal velocities are initialised as $v_{\mathrm{th}}^{\mathrm{swp}}/v_A = 0.4$, $v_{\mathrm{th}}^{\mathrm{swp}}/v_A = 1.2$, and $v_{\mathrm{th}}^{\mathrm{swp}}/v_A = 0.2$. The sets of relative densities and electron temperatures used for simulations presented in this paper are given in Table 1. For these simulations, the shear velocity of the magnetospheric populations is given by $u_{\mathrm{msp}} = u_{\mathrm{Na}} = 0$, and the shear velocity of the solar wind population is given by $u_{\mathrm{swp}} = -0.02v_A$.

The simulations are conducted using a Cartesian grid with 256 cells in x and y, with resolution $\Delta x, y = 0.5d_p$. We make use of 1500 computational particles per cell per species to sufficiently sample the distribution function in the tail regions of velocity space. A diagram of the simulation geometry is shown in Figure 1. Each simulation includes two shear boundaries centred at $x_0 = 64d_p$ and $x_1 = 192d_p$, as necessitated by our use of doubly periodic boundary conditions. The simulation grid is large enough that there is no significant transport of plasma across the boundary at $x = 0$ within the timescales discussed in this paper. That is, the vortices generated by the K-H instability at the dusk shear boundary do not interact with those at the dawn boundary. We note that for the initial conditions and parameters discussed in this section, the shear boundary at $x_0 = 64d_p$ has vorticity anti-parallel to the background magnetic field and associated ion gyration, and is termed the "counter-rotating" boundary. At $x_1 = 192d_p$, the vorticity is parallel to the background magnetic field, and is termed the "co-rotating" boundary. For northward IMF, the counter-rotating boundary corresponds to the dusk flank of Mercury's magnetosphere, and the co-rotating boundary corresponds to the dawn flank.

The simulation geometry described above constitutes a localised treatment of the magnetospheric boundary layers. In contrast to a full global simulation, we are therefore neglecting the effects of magnetic curvature, interactions with the planetary surface, and other complex features of the magnetic topology. However, our local approach allows us to more easily isolate the effect of high energy sodium ions on the evolution of K-H unstable boundaries, and the mechanism behind the interaction, at high spatio-temporal resolution.

3. Results

The following sections present an account of the evolutionary features in our simulations.

3.1. Kelvin-Helmholtz Instability

The time evolution of the number density of solar wind protons is shown for simulations of varying peak sodium number density n_0^{Na} in Figure 2. Several important features emerge from comparison between the simulations shown, including:

1. Waves associated with the Kelvin-Helmholtz instability are seen to grow at both shear boundaries at early times, forming characteristic rolled-up vortices clearly visible, for example, at $t = 80t_\Omega$ for $n_0^{\mathrm{Na}} = 0.5$ in Figure 2.

2. For all simulations, the growth of vortices on the dawn side shear boundary (right hand boundary) is suppressed compared to the dusk boundary for the same initial conditions. For high sodium ion densities, no coherent vortices form at the dawn, co-rotating boundary at all, as is perhaps most clear at $t = 320t_\Omega$ for $n_0^{\mathrm{Na}} = 1$ in Figure 2.

3. As the number density of the sodium ion population is increased, the growth rate of the K-H instability is increased at the dusk side boundary, and decreased at the dawn side boundary.

4. Increases in the magnetospheric sodium ion density can affect the scales sizes of the fastest growing modes of the K-H instability, resulting in differences in the size of vortices. This effect can be clearly seen in comparison of the dusk boundaries at $t = 160t\Omega$ for $n_0^{\mathrm{Na}} = 0$ and 0.5.

5. The density enhancements parallel to the y-axis are associated with transient fast mode waves, as mentioned in Section 2.

We show the dependence of the growth rate of the Kelvin-Helmholtz instability on sodium ion density at dusk and dawn boundaries in Figure 3. The growth rate of the K-H instability is higher at the dusk boundary than the dawn boundary for all sodium ion densities, which agrees with the MESSENGER results. Importantly, the change in growth rate due to differences in the initial conditions between simulations, i.e. the sodium ion density and electron temperature, are shown to have a much smaller effect on the growth rate of K-H waves than the direction of ion gyration. This dominant change in the growth rate of the K-H instability with the direction of ion gyration demonstrates that kinetic effects play an important role in the evolution of magnetospheric shear boundaries. Indeed, the dependence of the growth rate on ion gyro-radius is well known to have an important effect based on linear analysis [Nagano, 1979] and simulation data (e.g. [Thomas & Winske, 1993; Nakamura et al., 2010; Henri et al., 2013]). However, it has been shown that the growth rate may be enhanced (or suppressed) at either the dusk or dawn boundary depending on the local plasma beta [Huba, 1996]. Given this variation, the mechanism which allows ion gyration to enhance or suppress the instability is not yet clear. Some simulations of kinetic scale boundaries suggest that suppression of K-H at co-rotating boundaries may be a result of a widening of the boundary layer to achieve kinetic equilibrium [Nakamura et al., 2010]. Indeed, widening of the boundary layer to approximately twice the initial width is visible at the dawn boundary at early times. Importantly, the wider dawn boundary and first K-H waves have scale lengths much less than the sodium ion gyro-radius, and hence we can expect sodium kinetic effects to be important to both dawn and dusk shear boundaries.

In Figure 4 we examine the time evolution of the power spectrum of fluctuations in the motional electric field E_y, in order to address this question in the context of the K-H instability in Mercury's magnetotail. These electric field fluctuations are associated with cross-boundary bulk velocities within K-H vortices.

In support of the observations of the proton number density in Figure 2, we see that in each case the power in the instability at the dawn, co-rotating boundary is lower than at the dusk-boundary across all scales. On the dusk boundaries, we can also see the transfer of power from small to large scales as K-H vortices grow. At early times for the dusk boundaries, we see an increase in power at proton gyro-scales. At later times, most importantly, we see even greater increases in power in the instability at modes with wavelengths of approximately the sodium gyro-radius. These sharp peaks coincide with periods in the evolution associated with strongly coherent vortices, as seen, for example, at $t = 160t_\Omega$ for $n_0^{\mathrm{Na}} = 0.5$ in Figure 2. This suggests that a resonance between sodium ion gyration and the Kelvin-Helmholtz vortices is an important contributor to the dynamics and evolution of the system, even for low sodium ion densities, strongly enhancing the asymmetry between the dusk and dawn flanks of the magnetotail. We examine the mechanism behind this gyro-resonance in the following section.

3.2. Vortex Gyro-resonance

In order to determine the mechanism responsible for the observed resonance between K-H vortices and sodium ion gyration, we perform test particle simulations representing the interaction of a low number density ion species (i.e. sodium ions) with fixed electromagnetic fields associated with a K-H vortex in the higher number density background population (i.e. the protons). Hence, we examine only the trajectories and bulk properties of the sodium ion population in a dominant proton plasma background, and neglect the self-consistent interaction of ion species to simplify the problem. With fixed, perpendicular magnetic field B_0, the convective electric field $\mathbf{E} = -\mathbf{u} \times \mathbf{B}$ is set up to represent a shear boundary with a superimposed vortex of varying radius. The non-zero background electromagnetic fields are therefore given by:

$$
\begin{aligned}
B_z &= (-1)^m B_0, && (5)\\
E_x &= (-1)^{m+1} r^2 \exp(-r^2/R_v^2)\sin\theta && (6)\\
&\quad +(-1)^{m+1} E_{\mathrm{drift}}(x-x_0)/|x-x_0|, &&\\
E_y &= (-1)^{m+1} r^2 \exp(-r^2/R_v^2)\cos\theta, && (7)
\end{aligned}
$$

where polar coordinates $r^2 = (x-x_0)^2 + (y-y_0)^2$ and $\tan\theta = (y-y_0)/(x-x_0)$ are taken relative to the centre of the vortex at $(x_0, y_0) = (100d_\mathrm{p}, 600d_\mathrm{p})$, and the shear boundary centred at $x = x_0$. Parameter R_v determines the radius of the vortex, which is co-rotating for $m = 1$ and counter-rotating for $m = 0$. A total of 10^5 particles are initialised with Maxwellian thermal velocity distribution and $\mathbf{E}\times\mathbf{B}$ drift v_d in a region upstream of the vortex with $x > x_0$, of size $3R_v + 2\rho_\mathrm{Na}$ in x, and $40\rho_\mathrm{Na}$ in y. This samples a population of interacting and non-interacting sodium ions on the magnetospheric side of the shear boundary, represented in Figure 1 by a hatched grey box. These test particles drift towards the stationary vortex and interact if their trajectories intersect the region for which the vortex electric field is significant. We track both interacting and non-interacting particle trajectories in order to better understand the interaction.

The time evolution of the one-dimensional number density $n(y)$ for test particles interacting with a vortex of varying radius and vorticity direction are shown in Figure 5. In panel (a), which shows results for a counter-rotating vortex with $R_v = \rho_\mathrm{Na}$, test particles are seen to drift towards the vortex and, after interaction at approximately $t = 0.7t_\Omega$, continue with the same drift velocity. This behaviour manifests as a largely unbroken diagonal line in (y, t). Results in panel (b), for a counter-rotating vortex with $R_v = 2\rho_{\rm Na}$, demonstrate that although non-interacting test particles continue to drift with the local shear velocity, many become trapped within the vortex. This behaviour manifests as a horizontal bar at the vortex's centre $y = y_0$. Panels (a) and (b) therefore demonstrate that test particles become trapped within the counter-rotating vortices provided they are larger than approximately twice the test particle gyro-radius (i.e. $R_v > \rho_{\rm Na}$). At a co-rotating boundary of radius $R_v = 2\rho_{\rm Na}$, as seen in panel (c), no test particles become trapped. Sodium ions are instead deflected around the vortex before continuing to drift with the local shear velocity. Hence, sodium ions cannot continue to interact with the vortex for a time longer than $\approx 2R_v/v_d$. We note that this behaviour leads to a modulation of particle trajectories in gyro-phase, visible as periodic peaks in the number density after interaction with the vortex.

The differences in the interaction of test particles with co- and counter-rotating vortices can be seen clearly in the particle trajectories, shown in Figure 6. For a typical trajectory for the co-rotating case (shown in blue), we observe a deflection of intersecting test particles in the outward direction from the vortex centre, leading to an azimuthal drift of test particles around the vortex. For the counter-rotating case (shown in red), test particles which intersect with the vortex are accelerated towards the centre of the vortex by the radial motional electric field, and become trapped in a precessing petal orbit with scale size equal to the vortex radius. Although the gyration of these particles is in the opposite direction to the background vorticity, these particles contribute a co-rotating current, as shown in Figure 7. This co-rotating current increases the power in the counter-rotating K-H vortex, leading to the observed gyro-resonance in Figure 4.

3.3. Ion Transport

In this section we examine the effect of sodium ion density on the transport of protons and sodium ions across the magnetopause. Having calculated the mean-square displacement of a chosen population of ions $\langle \Delta x_s^2 \rangle$, we can characterise the time evolution by defining a diffusion coefficient D_s as follows:

$$D_s = \frac{\langle \Delta x_s^2 \rangle}{t}. \tag{8}$$

We can then test for a power law increase in mean-square displacement such that $\langle \Delta x_s^2 \rangle \propto (\Omega_s t)^\gamma$. For classical diffusion, $\gamma = 1$ and the diffusion coefficient D is constant. Plots of the time evolution of the mean square displacement for ions initialised within $10 d_i$ of each boundary are shown in Figure 8. The curves demonstrate hyper-diffusive power laws $\gamma > 1$ apply for both dawn and dusk boundaries in all simulations. With no sodium ion impurity, the exponent γ is higher at the dawn flank. However, increasing the sodium ion density decreases the transport exponent at the dawn flank, but has little effect on the dusk flank. This implies that the suppression of the growth of K-H vortices at the dawn flank by the sodium ion population reduces the cross-boundary transport of plasma in that region.

Ion transport can also be quantified by considering a "mixing parameter", M, defined as the fraction of computational cells in the simulation domain with a given minimum number density of both magnetospheric and solar wind protons:

$$M = \sum_i f_i / N_{\text{cells}}, \tag{9}$$

for a sum over all computational cells i, with total cells N_{cells}. The conditional function f_i for cell i is given by:

$$f_i = \begin{cases} 1, & \text{if } \left(n_i^{\text{swp}} \geq \frac{1}{2} n_0^{\text{swp}}\right) \;\&\; \left(n_i^{\text{msp}} \geq \frac{1}{2} n_0^{\text{msp}}\right) \\ 0, & \text{otherwise.} \end{cases} \tag{10}$$

Plots of the time evolution of the mixing parameter M for the simulations discussed in this paper are shown in Figure 9. These plots demonstrate that the mixing rate is higher at the dusk boundary than the dawn boundary for both proton and sodium ion populations. Additionally, increasing the sodium ion density appears to increase the mixing rate of the sodium with solar wind protons at both flanks. Together with the results in Figure 8, this implies that the growth of coherent vortices at the dusk boundary, and the suppression of the K-H instability at the dawn flank, leads to faster cross-boundary transport and more efficient mixing at the dusk flank.

4. Conclusions

Our simulations have reproduced the strong dusk-dawn asymmetry in the growth of the Kelvin-Helmholtz instability observed in both global hybrid simulations [Trávníček et al., 2009; Paral & Rankin, 2013] and observational data from the MESSENGER spacecraft [Liljeblad et al., 2014; Sundberg et al., 2012]. We have further demonstrated that it is necessary to consider the effect of low density, massive ion species of exospheric origin if we are to properly model the growth and evolution of plasma instabilities in the local Hermean plasma environment.

We have shown that the inclusion of a hot sodium ion population introduces a resonance between K-H vortices and ion gyration. Our results are consistent with the observations of Gershman et al. [2015], who report high correlation between K-H wave frequency and sodium gyro-frequency in the dusk magnetotail. In out simulations, this manifests as a strong spectral peak in K-H wave power close to sodium gyro-scales, corresponding to highly coherent, persistent vortices visible at the sodium gyroradius at dusk, counter-rotating boundaries. In contrast, the inclusion of sodium ions leads to almost complete suppression of vortex growth at dawn, co-rotating boundaries.

Test particle simulations suggest that the source of the gyro-resonance at dusk boundaries is the generation of a co-rotating current formed by the combination of petal-like orbits of counter-rotating sodium ions trapped in K-H vortices.

An analysis of diffusion power laws and mixing parameters has shown that ion transport is faster at dusk boundaries than at the dawn flank in the presence of sodium ions, and that the dusk flank plasma is more highly mixed than at the dawn flank. This suggests that the growth of gyro-resonant, coherent K-H vortices leads to a more efficient mixing of the solar wind and magnetospheric populations, and that suppression of the K-H instability reduces cross-boundary transport.

Although local plasma simulations provide an ideal environment for the study of highly specific plasma processes, as in this paper, high-resolution global simulations may still be necessary to determine the importance of sodium ion gyro-resonance to Mercury's local plasma environment. For example, a more realistic, three-dimensional geometry will enable the assessment of the impact of magnetic reconnection in K-H vortices, which can accelerate and heat both proton and sodium ion populations. Non-periodic boundary conditions representing the interaction of the magnetospheric plasma with the planetary surface may also be necessary to more robustly predict the evolution of the Kelvin-Helmholtz instability and other boundary layer instabilities. Finally, though the K-H instability grows self-consistently from grid-scale noise in the simulations presented in this paper, a more realistic model of a magnetosphere may also include K-H waves initialised by high amplitude solar wind perturbations and fluctuations in the magnetosheath dynamic pressure. In such cases, the gyro-resonance mechanism we have discussed can be expected to operate for perturbations of scale length less than the sodium gyro-radius. However, suppression of the growth of vortices on the dawn shear boundary may be overcome with sufficient driving. These considerations will be important to direct comparison of three-dimensional, global simulations of vortex gyro-resonance at the magnetopause with observational data.

Acknowledgments.

This work was supported by the UK Science and Technology Facilities Council grant ST/J001546/1, and the European Commissions Seventh Framework Programme FP7 under the grant agreement SHOCK (project number 284515). This work used the DiRAC Complexity system, operated by the University of Leicester IT Services, which forms part of the STFC DiRAC HPC Facility (www.dirac.ac.uk). This equipment is funded by BIS National E-Infrastructure capital grant ST/K000373/1 and STFC DiRAC Operations grant ST/K0003259/1. DiRAC is part of the National E-Infrastructure. Simulation data is available upon request (p.w.gingell@qmul.ac.uk).

References

Anderson, B. J., M. H. Acuña, H. Korth, et al. (2008), The Structure of Mercury's Magnetic Field from MESSENGER's First Flyby, Science, 321, 82, doi:10.1126/science.1159081

Boardsen, S. A., T. Sundberg, J. A. Slavin, et al. (2010), Observations of Kelvin-Helmholtz waves along the dusk-side boundary of Mercury's magnetosphere during MESSENGER's third flyby, *Geophys. Res. Lett.,* , 37, 12101, doi:10.1029/2010GL043606

Cerri, S. S., P. Henri, F. Califano, et al. (2013), Extended fluid models: Pressure tensor effects and equilibria, Physics of Plasmas, 20, 112112, doi:10.1063/1.4828981

Chandrasekhar, S. (1961), Hydrodynamic and hydromagnetic stability, International Series of Monographs on Physics, Oxford

Chen, S.-H., & M. G. Kivelson (1993), On nonsinusoidal waves at the Earth's magnetopause, *Geophys. Res. Lett.,* , 20, 2699, doi:10.1029/93GL02622

Chen, S.-H., M. G. Kivelson, J. T. Gosling, R. J. Walker, & A. J. Lazarus (1993), Anomalous aspects of magnetosheath flow and of the shape and oscillations of the magnetopause during an interval of strongly northward interplanetary magnetic field, *J. Geophys. Res.,* , 98, 5727, doi:10.1029/92JA02263

Delamere, P. A., R. J. Wilson, & A. Masters (2011), Kelvin-Helmholtz instability at Saturn's magnetopause: Hybrid simulations, Journal of Geophysical Research (Space Physics), 116, 10222, doi:10.1029/2011JA016724

Fairfield, D. H., A. Otto, T. Mukai, et al. (2000), Geotail observations of the Kelvin-Helmholtz instability at the equatorial magnetotail boundary for parallel northward fields, *J. Geophys. Res.,* , 105, 21159, doi:10.1029/1999JA000316

Fairfield, D. H., C. J. Farrugia, T. Mukai, T. Nagai, & A. Fedorov (2003), Motion of the dusk flank boundary layer caused by solar wind pressure changes and the Kelvin-Helmholtz instability: 10-11 January 1997, Journal of Geophysical Research (Space Physics), 108, 1460, doi:10.1029/2003JA010134

Fairfield, D. H., M. M. Kuznetsova, T. Mukai, et al. (2007), Waves on the dusk flank boundary layer during very northward interplanetary magnetic field conditions: Observations and simulation, Journal of Geophysical Research (Space Physics), 112, 8206, doi:10.1029/2006JA012052

Farrugia, C. J., F. T. Gratton, J. Contin, et al. (2000), Coordinated Wind, Interball/tail, and ground observations of Kelvin-Helmholtz waves at the near-tail, equatorial magnetopause at dusk: January 11, 1997, *J. Geophys. Res.,* , 105, 7639, doi:10.1029/1999JA000267

Gershman, D. J., J. A. Slavin, J. M. Raines, et al. (2014), Ion kinetic properties in Mercury's pre-midnight plasma sheet, *Geophys. Res. Lett.,* , 41, 5740, doi:10.1002/2014GL060468

Gershman, D. J., J. M. Raines, J. A. Slavin, et al. (2015), MESSENGER observations of multi-scale Kelvin-Helmholtz vortices at Mercury, Journal of Geophysical Research: Space Physics, doi:10.1002/2014JA020903

Gingell, P. W., S. C. Chapman, & R. O. Dendy (2014), Plasma blob formation by ion kinetic Kelvin-Helmholtz and interchange instabilities, Plasma Physics and Controlled Fusion, 56, 035012, doi:10.1088/0741-3335/56/3/035012

Hasegawa, H., M. Fujimoto, T.-D. Phan, et al. (2004), Transport of solar wind into Earth's magnetosphere through rolled-up Kelvin-Helmholtz vortices, Nature, 430, 755, doi:10.1038/nature02799

Henri, P., S. S. Cerri, F. Califano, et al. (2013), Nonlinear evolution of the magnetized Kelvin-Helmholtz instability: From fluid to kinetic modeling, Physics of Plasmas, 20, 102118, doi:10.1063/1.4826214

Huba, J. D. 1996, The Kelvin-Helmholtz instability: Finite Larmor radius magnetohydrodynamics, *Geophys. Res. Lett.,* , 23, 2907, doi:10.1029/96GL02767

Hwang, K.-J., M. M. Kuznetsova, F. Sahraoui, et al. (2011), Kelvin-Helmholtz waves under southward interplanetary magnetic field, Journal of Geophysical Research (Space Physics), 116, 8210, doi:10.1029/2011JA016596

Kokubun, S., H. Kawano, M. Nakamura, et al. (1994), Quasi-periodic oscillations of the magnetopause during northward sheath magnetic field, *Geophys. Res. Lett.,* , 21, 2883, doi:10.1029/94GL02103

Liljeblad, E., T. Sundberg, T. Karlsson, & A. Kullen (2014), Statistical investigation of Kelvin-Helmholtz waves at the magnetopause of Mercury, Journal of Geophysical Research (Space Physics), 119, 9670, doi:10.1002/2014JA020614

Masters, A., N. Achilleos, C. Bertucci, et al. (2009), Surface waves on Saturn's dawn flank magnetopause driven by the Kelvin-Helmholtz instability, Planetary Space Science, 57, 1769, doi: 10.1016/j.pss.2009.02.010

Masters, A., N. Achilleos, M. G. Kivelson, et al. (2010), Cassini observations of a Kelvin-Helmholtz vortex in Saturn's outer magnetosphere, Journal of Geophysical Research (Space Physics), 115, 7225, doi:10.1029/2010JA015351

Matthews, A. P. (1994), Current Advance Method and Cyclic Leapfrog for 2D Multispecies Hybrid Plasma Simulations, Journal of Computational Physics, 112, 102, doi:10.1006/jcph.1994.1084

Nagano, H. (1979), Effect of finite ion Larmor radius on the Kelvin-Helmholtz instability of the magnetopause, Planetary Space Science, 27, 881, doi:10.1016/0032-0633(79)90013-8

Nakamura, T. K. M., H. Hasegawa, & I. Shinohara (2010), Kinetic effects on the Kelvin-Helmholtz instability in ion-to-magnetohydrodynamic scale transverse velocity shear layers: Particle simulations, Physics of Plasmas, 17, 042119, doi:10.1063/1.3385445

Otto, A., & D. H. Fairfield (2000), Kelvin-Helmholtz instability at the magnetotail boundary: MHD simulation and comparison with Geotail observations, *J. Geophys. Res.,* , 105, 21175, doi:10.1029/1999JA000312

Paral, J., & R. Rankin (2013), Dawn-dusk asymmetry in the Kelvin-Helmholtz instability at Mercury, Nature Communications, 4, 1645, doi:10.1038/ncomms2676

Pope, S. A., M. A. Balikhin, T. L. Zhang, et al. (2009), Giant vortices lead to ion escape from Venus and re-distribution of plasma in the ionosphere, *Geophys. Res. Lett.,* , 36, 7202, doi:10.1029/2008GL036977

Raines, J. M., J. A. Slavin, T. H. Zurbuchen, et al. (2011), MESSENGER observations of the plasma environment near Mercury, Planetary Space Science, 59, 2004, doi:10.1016/j.pss.2011.02.004

Slavin, J. A., M. H. Acuña, B. J. Anderson, et al. (2008), Mercury's Magnetosphere After MESSENGER's First Flyby, Science, 321, 85, doi:10.1126/science.1159040

Slavin, J. A., M. H. Acuña, B. J. Anderson, et al. (2009), MESSENGER Observations of Magnetic Reconnection in Mercury's Magnetosphere, Science, 324, 606, doi:10.1126/science.1172011

Sundberg, T., S. A. Boardsen, J. A. Slavin, L. G. Blomberg, & H. Korth (2010), The Kelvin-Helmholtz instability at Mercury: An assessment, Planetary Space Science, 58, 1434, doi:10.1016/j.pss.2010.06.008

Sundberg, T., S. A. Boardsen, J. A. Slavin, et al. (2011), Reconstruction of propagating Kelvin-Helmholtz vortices at Mercury's magnetopause, Planetary Space Science, 59, 2051, doi:10.1016/j.pss.2011.05.008

Sundberg, T., S. A. Boardsen, J. A. Slavin, et al. (2012), MESSENGER orbital observations of large-amplitude Kelvin-Helmholtz waves at Mercury's magnetopause, Journal of Geophysical Research (Space Physics), 117, 4216, doi:10.1029/2011JA017268

Thomas, V. A. (1995), Three-dimensional kinetic simulation of the Kelvin-Helmholtz instability, *J. Geophys. Res.,* , 100, 19429, doi:10.1029/95JA01130

Thomas, V. A., & D. Winske (1991), Kinetic simulation of the Kelvin-Helmholtz instability at the Venus ionopause, *Geophys. Res. Lett.,* , 18, 1943, doi:10.1029/91GL02552

Thomas, V. A., & D. Winske (1993), Kinetic simulations of the Kelvin-Helmholtz instability at the magnetopause, *J. Geophys. Res.,* , 98, 11425, doi:10.1029/93JA00604

Trávníček, P. M., P. Hellinger, D. Schriver, et al. (2009), Kinetic instabilities in Mercury's magnetosphere: Three-dimensional simulation results, *Geophys. Res. Lett.,* , 36, 7104, doi:10.1029/2008GL036630

Zurbuchen, T. H., J. M. Raines, G. Gloeckler, et al. (2008), MESSENGER Observations of the Composition of Mercury's Ionized Exosphere and Plasma Environment, Science, 321, 90, doi:10.1126/science.1159314

Zurbuchen, T. H., J. M. Raines, J. A. Slavin, et al. (2011), MESSENGER Observations of the Spatial Distribution of Planetary Ions Near Mercury, Science, 333, 1862,

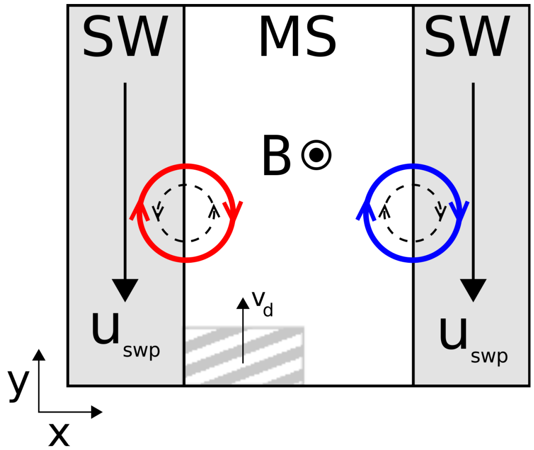

Figure 1. Diagram of the geometry of the initial conditions used for simulations discussed in this paper. Shear boundaries separating the solar wind (SW) and magnetopsheric (MS) populations are shown with coloured circles corresponding to the direction of gyration of co-rotating (blue) and counter-rotating (red) ions. Dashed circles demonstrate the direction of bulk flow within vortices generated by the K-H instability at each shear boundary. Note that the relation between the direction of gyration (coloured circles) and vorticity (dashed circles) determines which boundary is co-rotating and which is counter-rotating. The hatched grey box represents the initial position of the test particle population discussed in Section 3.2.

Table 1. List of simulation parameters, including peak magnetospheric proton density n_0^{msp}, peak solar wind proton density n_0^{swp}, peak sodium ion density n_0^{Na} and dimensionless electron temperature $\tau_e = 2\beta_e$.

n_0^{msp}/n_0	n_0^{swp}/n_0	n_0^{Na}/n_0	τ_e
1	4	0	0.133
1	4	0.1	0.154
1	4	0.5	0.252
1	4	1	0.430

448 doi:10.1126/science.1211302

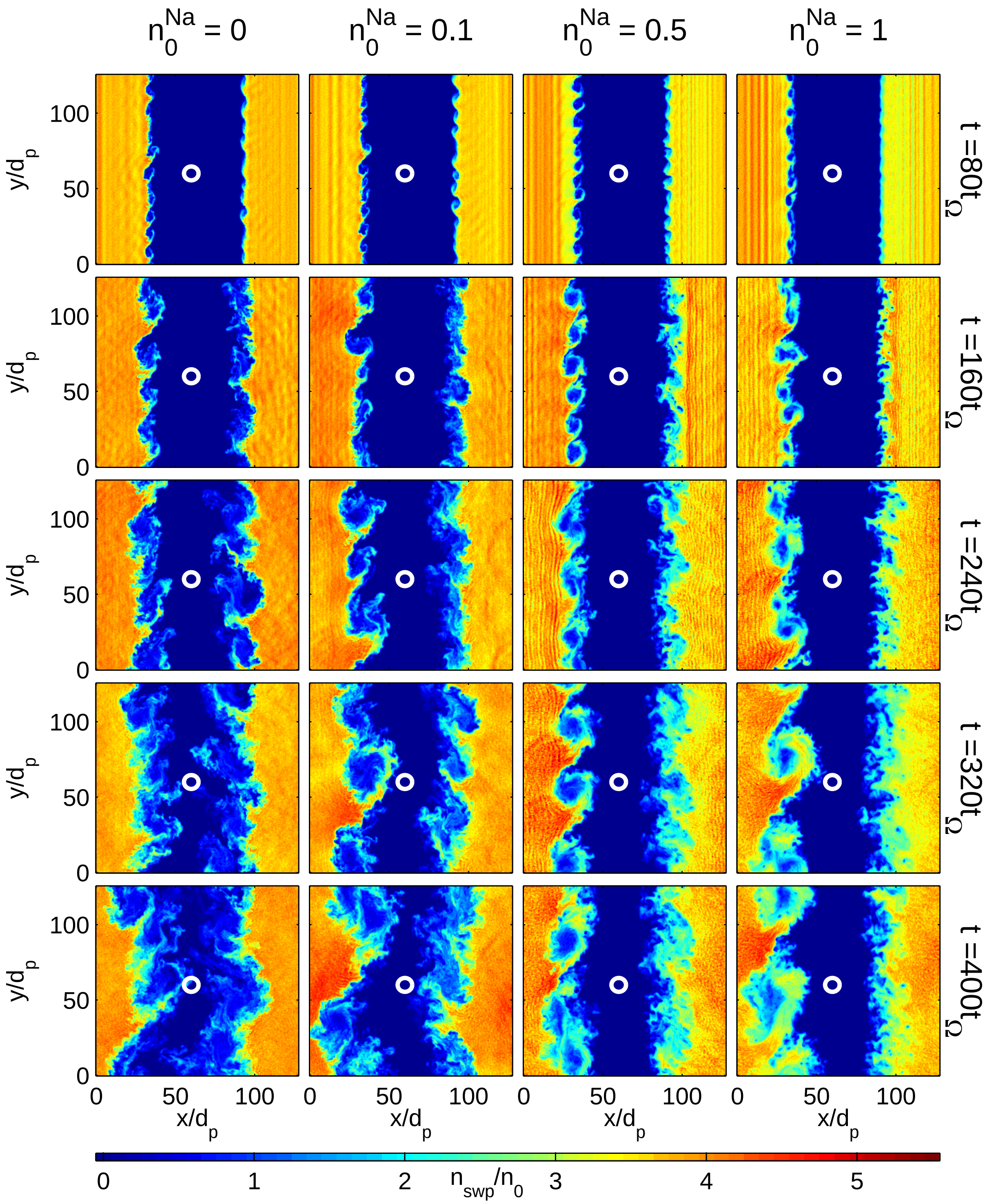

Figure 2. The time evolution of the number density of solar wind protons, for simulations with $n_0^{\mathrm{Na}} = (0, 0.1, 0.5, 1)$ left to right. Note that an increase in the number density of sodium ions in the magnetospheric population leads to a strong asymmetry in the growth of the Kelvin-Helmholtz instability between the dusk and dawn shear boundaries. The thermal gyro-radius of the sodium ion population is represented with a white circle.

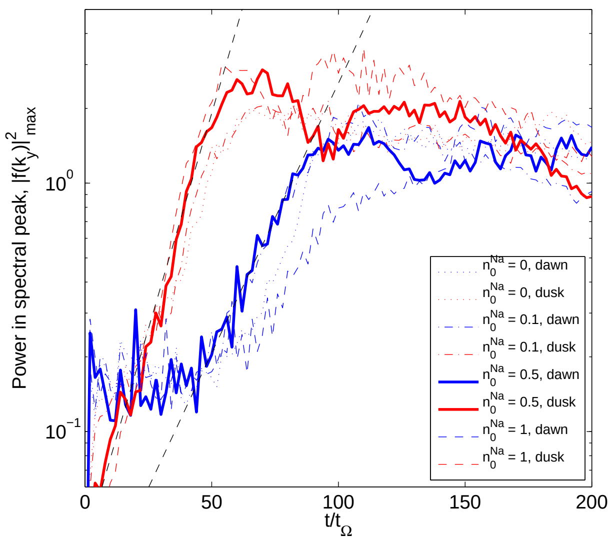

Figure 3. Peak power in the spectrum of K-H waves, from cross-boundary motional electric field E_y, for dusk (red) and dawn (blue) boundaries. For dusk, counter-rotating boundaries, the growth rate of the K-H instability is both faster, and begins at an earlier time. However, there is no definitive trend in the change in growth rate caused by sodium ion density at either boundary.

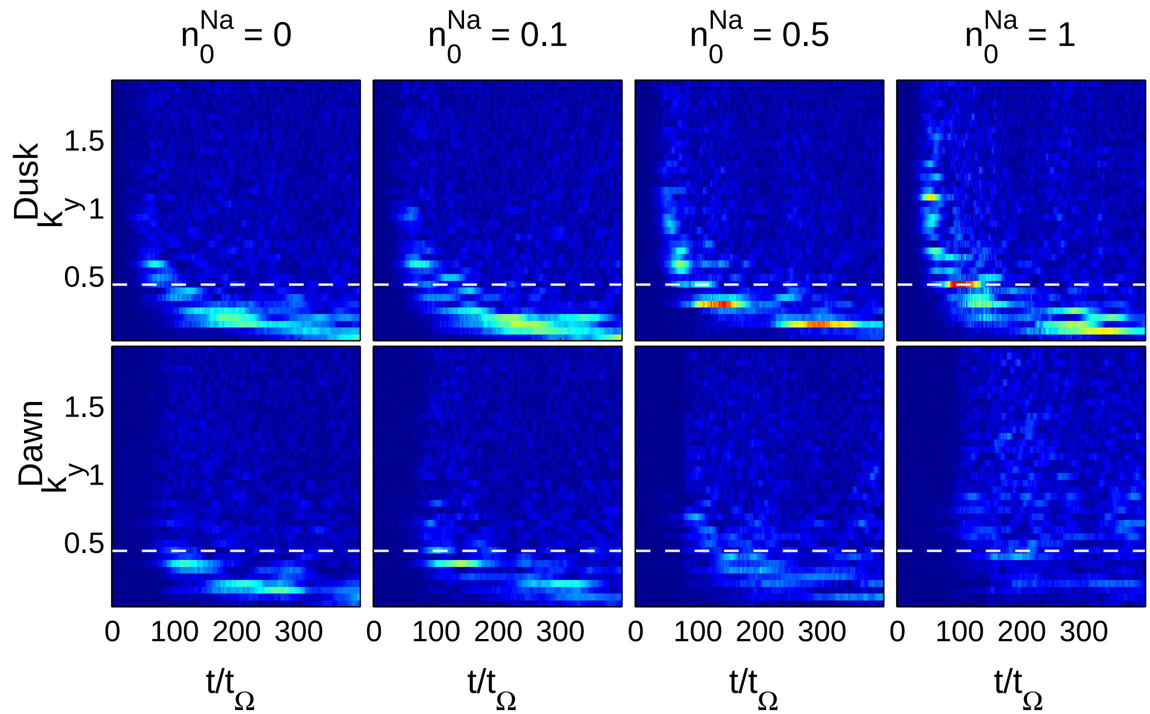

Figure 4. The time evolution of power spectral density of K-H waves from the field E_y at dusk (top) and dawn (bottom) boundaries, for increasing sodium ion density from left to right. Two important features emerge: i) increasing sodium ion density causes the suppression of waves across all scales at dawn boundaries and ii) increasing sodium ion density introduces spectral features at sodium gyro-scales. The sodium ion gyro-radius is represented with a white dashed line.

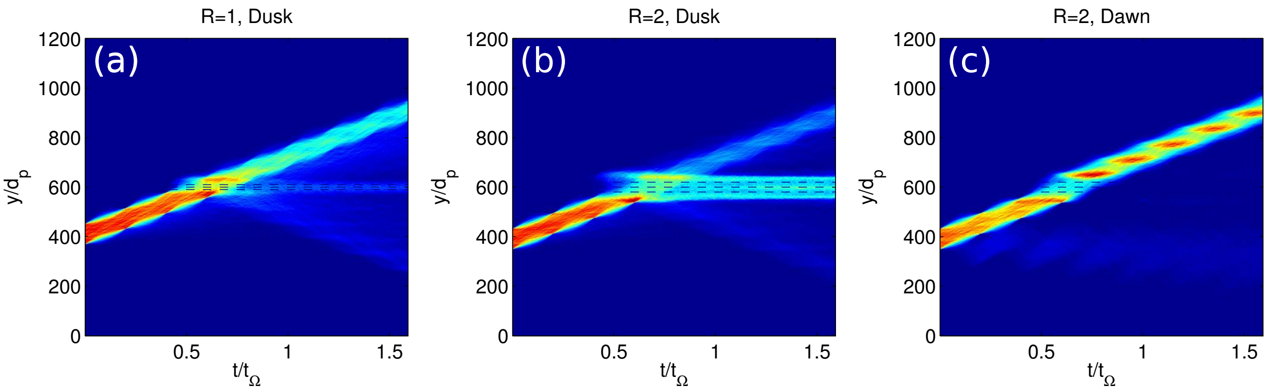

Figure 5. Histograms showing the time evolution of test particle number density for varying size and direction of imposed vortex, for a set of test particles initialised in the region $380 < y_0/d_p < 450$. Dashed lines represent the centres and radii of the vortices. For counter-rotating vortices above approximately twice the sodium gyro-radius, we see significant trapping of sodium ion within the vortex. For all sizes of co-rotating boundaries, sodium ions are deflected rather than trapped.

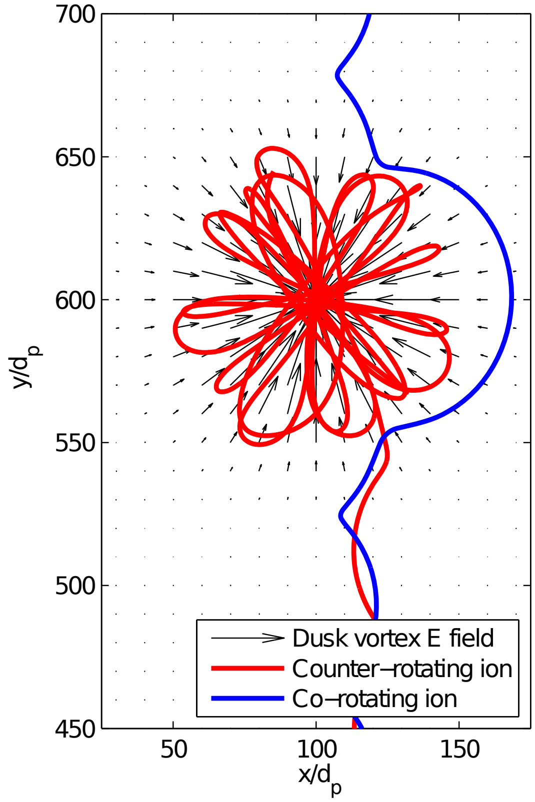

Figure 6. Examples of test particle trajectories for counter-rotating (red) and co-rotating (blue) vortices, corresponding to dusk and dawn shear boundaries respectively. These trajectories demonstrate the characteristic petal-shaped orbit of a trapped counter-rotating ion and deflection of a co-rotating ion.

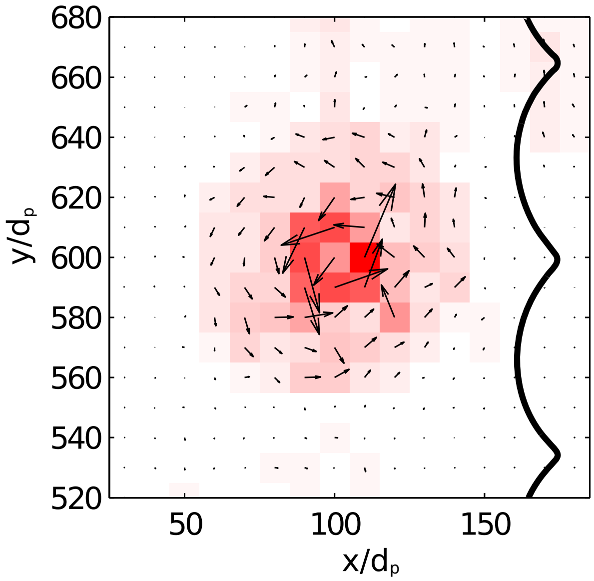

Figure 7. Magnitude (colour) and direction (arrows) of the contribution of test particles to the current for a counter-rotating shear boundary. A sample background ion trajectory is shown in black. Note that the direction of the total current of the sodium ion population is co-rotating with the vortex, despite the counter-rotation of the individual particle gyration.

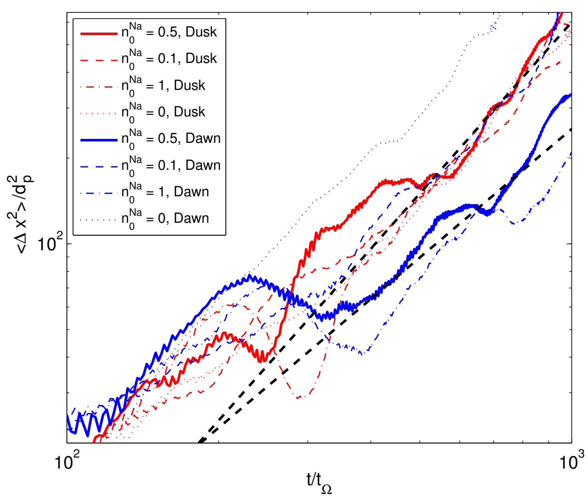

Figure 8. Mean square ion displacement, $\langle \Delta x_s^2 \rangle$, for solar wind protons at dusk (red) and dawn (blue) boundaries with varying sodium ion number density. Although proton transport appears unaffected by sodium density at the dusk boundary, introduction of sodium at the dawn boundary is seen the reduce transport. Two dashed black lines represent power laws with exponents $\gamma = 2$ and $\gamma = 1.5$.

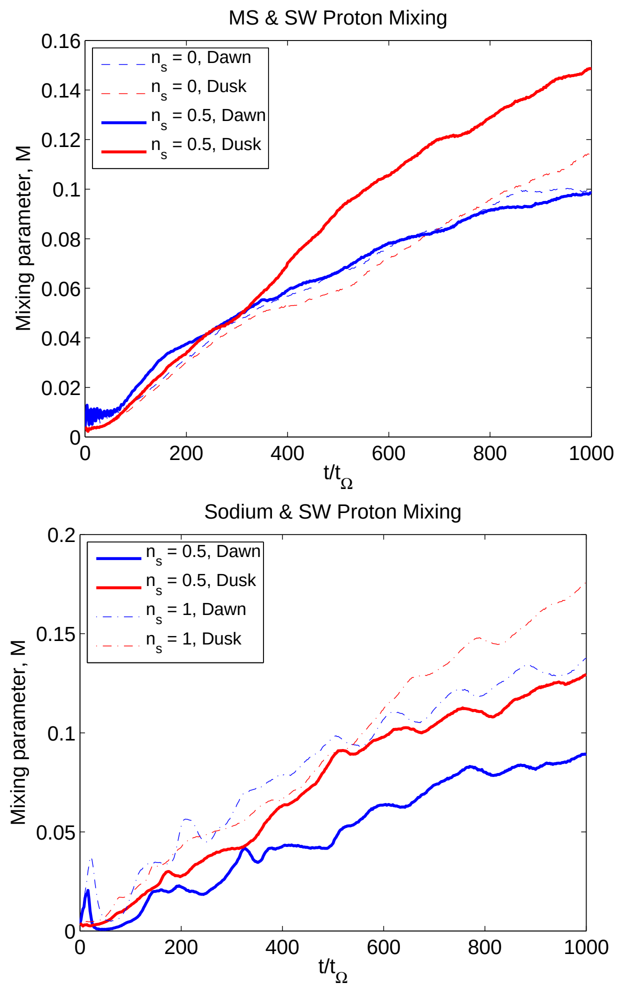

Figure 9. Time evolution of the mixing parameters for magnetospheric and solar wind protons (top), and for sodium ion and solar wind protons (bottom). In both cases, the plasma at the dusk boundaries are seen to be more highly mixed than their dawn counterparts with the introduction of a sodium ion population.